Comparative Medicine
Copyright 2023
by the American Association for Laboratory Animal Science

Vol 73, No 4
August 2023
Pages 311–322

Original Research

Mitigation of Fibrosis after Myocardial Infarction in Rats by Using a Porcine Cholecyst Extracellular Matrix

Reshma S Nair,[1,†] Praveen K Sobhan,[2] Sachin J Shenoy,[3] Mukund A Prabhu,[4,‡] Vikas Kumar,[5,§] Surya Ramachandran,[5] and Thapasimuthu V Anilkumar[1,*]

Fibrosis that occurs after nonfatal myocardial infarction (MI) is an irreversible reparative cardiac tissue remodeling process characterized by progressive deposition of highly cross-linked type I collagen. No currently available therapeutic strategy prevents or reverses MI-associated fibrotic scarring of myocardium. In this study, we used an epicardial graft prepared of porcine cholecystic extracellular matrix to treat experimental nonfatal MI in rats. Graft-assisted healing was characterized by reduced fibrosis, with scanty deposition of type I collagen. Histologically, the tissue response was associated with a favorable regenerative reaction predominated by CD4-positive helper T lymphocytes, enhanced angiogenesis, and infiltration of proliferating cells. These observations indicate that porcine cholecystic extracellular matrix delayed the fibrotic reaction and support its use as a potential biomaterial for mitigating fibrosis after MI. Delaying the progression of cardiac tissue remodeling may widen the therapeutic window for management of scarring after MI.

Abbreviations: C-ECM, cholecystic extracellular matrix; ECM, extracellular matrix; MI, myocardial infarction; PCNA, proliferating cell nuclear antigen

DOI: 10.30802/AALAS-CM-22-000097

Introduction

Myocardial infarction is essentially coagulative necrosis of the muscular wall of heart due to ischemia, usually occurring after partial or complete occlusion of coronary blood vessels.[2] In the absence of inadequate reperfusion, replacement of the necrotic myocardium with collagen-rich scar tissue happens as a reparative tissue remodeling process.[57] Surgical treatment strategies for managing MI include percutaneous coronary intervention and coronary artery bypass graft surgery.[47] Independently or in parallel, the use of various therapeutic biomolecules (e.g., angiotensin converting enzyme, beta blockers, endothelin antagonists, statins) to minimize the chances of ischemia are being studied.[17] However, to date, none of these conventional or novel therapeutic strategies prevent the progression of the adverse remodeling of ventricular fibrotic cardiac tissue.[4] Therefore, attenuating scar formation is considered a desirable strategy in long-term management of MI.[21] In this regard, any drug, device, or method that favors delayed scarring has paramount importance.

Emerging tissue engineering approaches in regenerative medicine that use cells,[10,15,27,41,58] regulatory (signaling) biomolecules,[16,46,60] and scaffolds[39,54,59] offer new avenues for better management of MI. Among these, the use of cells has not yet become a viable clinical management tool for treating MI because of several drawbacks, including the difficulty in acquiring sufficient numbers of cells, inefficient *ex vivo* expansion, lack of methods for onsite delivery, inefficient *in vivo* differentiation, lack of sustained regenerative potential, and inadequate integration with host tissue.[6] A second approach, the use of cell-regulatory biomolecules such as growth factors, has garnered some interest because of the direct action of these compounds on angiogenesis, extracellular matrix remodeling, cardiomyocyte proliferation and stem-cell recruitment;[62] however, their short biologic half-life, low plasma stability, and low specificity for targeting cell-specific epitopes limit their use in routine cardiac therapy.[46] Unlike cells and signaling biomolecules, tissue engineering scaffolds, especially xenogeneic extracellular matrices prepared by appropriate decellularization of mammalian organs or tissue, have been used as grafts for treating MI.[30] These cellular scaffolds are utilized for cardiac tissue engineering despite concerns regarding zoonosis[1] and graft rejection.[25] Although these engineered biomaterials do not themselves mitigate cardiac fibrosis, attempts are being made to modulate their properties by adding various biomolecules capable of minimizing fibrotic scar formation.[18,20,31,63] Therefore, graft-assisted healing of injured

Submitted: 27 Aug 2022. Revision requested: 27 Oct 2022. Accepted: 09 Dec 2022.
[1]Division of Experimental Pathology, [2]Division of Tissue Culture, [3]Division of In Vivo Models and Testing, Department of Applied Biology, Biomedical Technology Wing, Sree Chitra Tirunal Institute for Medical Sciences and Technology, Thiruvananthapuram, India; [4]Department of Cardiology, Sree Chitra Tirunal Institute for Medical Sciences and Technology, Thiruvananthapuram, India; [5]Cardiovascular Diseases and Diabetes Biology, Rajiv Gandhi Centre for Biotechnology, Thiruvananthapuram, India
Current affiliations: [†]Department of Biochemistry and Molecular Medicine, Université de Montréal and Montreal Heart Institute, Montréal, Québec, Canada; [‡]Department of Cardiology, Kasturba Medical College Manipal, Manipal Academy of Higher Education, Manipal, Karnataka; and [§]Diabetes Research Program, Department of Medicine, New York University School of Medicine, New York.
**Corresponding author. Email: tvanilkumar@sctimst.ac.in*

myocardium with both synthetic and nonsynthetic grafts is a promising treatment option.[9]

Acellular xenogeneic extracellular matrix (ECM)–based biomaterials—including those derived from porcine small intestinal submucosa, pericardium, and urinary bladder ECM—have been used as constructive scaffolds for regeneration in many tissues including the mural cardiac myocardium.[30,51] Such natural scaffolds are superior to synthetic scaffolds because the natural products elicit minimal unfavorable foreign-body giant-cell-mediated reaction.[1] Indeed, several bovine pericardium-based ECM scaffolds have been used in cardiac repair, but all have shown poor tissue integration.[42] In contrast, a porcine small-intestinal ECM recently became popular in cardiovascular tissue engineering because of its ease of use, remodeling properties, lack of immunogenicity, absorbability, and potential to promote native tissue growth.[32] However, none of these biomaterials mitigates replacement fibrosis after MI.

Against this background, we evaluated the use of a porcine cholecystic ECM (C-ECM) in the form of an epicardial graft for treating myocardial damage in a rat model of nonfatal MI. As a source organ for the preparation of ECM for xenogeneic grafting, porcine cholecyst (gall bladder) has clear advantages.[35] In addition, the preparation methods have been optimized;[11] in particular, the minimal use of detergents and chemicals allows retention of many endogenous biomolecules that promote wound healing.[33] As a biomaterial for graft-assisted healing, C-ECM promoted rapid healing of skin excisions,[49] burns,[48] and lacerations[24] in rabbits and dogs. Experiments in rats have shown that when used as a subcutaneous or skeletal muscle graft, C-ECM promotes an anti inflammatory reaction that is mediated by M2 macrophages.[5,37] Furthermore, the biocompatibility of C-ECM has been established through robust protocols described in ISO 10993.[3,5,37] In contrast to some currently available xenogeneic grafts, C-ECM promotes regenerative tissue remodeling reaction in animal models.[5,24,36] For example, studies using gelatin-modified C-ECM promoted angiogenesis and healing of diabetic wounds,[34] and use of a polypropylene mesh that was surface-modified with a C-ECM hydrogel mitigated host tissue reactions in rats.[45] We recently coated porcine C-ECM with gold nanoparticles, subsequently characterized the physicochemical and biologic properties of the modified material, and assessed its potential use as an epicardial graft.[39,40] The current study demonstrates the cardioprotective properties of porcine C-ECM and its ability to mitigate cardiac fibrosis after MI in rats.

Materials and Methods

Preparation of the scaffold. Porcine C-ECM was prepared by using a nondetergent, nonenzymatic method as previously described.[3] Briefly, porcine cholecysts were collected from a slaughterhouse, placed in 10% neutral buffered formaldehyde, and transferred to the laboratory. ECM was recovered manually by delamination of tissue layers after ex situ incubation of the source organ in the stabilizing agent for 30 to 36 h to allow *in situ* controlled cross-linking of biomolecules.[33] The C-ECM was subsequently preserved as thin (about 100 µm) lyophilized sheets. Sheets of C-ECM were packed in sterilization reels and sterilized through exposure to ethylene oxide gas at 37 °C and stored in a desiccator for future use.

Induction of MI in rats. The study was conducted with the approval of the Institutional Animal Ethics Committee as per the statutory regulations prescribed by the Committee for the Control and Supervision of Experiments on Animals (Government of India). Young adult Sprague–Dawley rats (240 to 290 g) were kept under the standard conditions of our institution (Sree Chitra Tirunal Institute for Medical Sciences and Technology, Thiruvananthapuram, India).

Rats were individually housed for one week prior to the day of surgery as part of acclimatization to the experimental setting. An individually-ventilated caging system (Citizen Industries, Ahmedabad, India) was used. Rats were housed in polysulfone cages with stainless steel 304 wire grill tops. Sterile corncob (Sparconn, Bangalore, India) was used as bedding material. Rats were fed *ad libitum* with pelleted feed (Safe rodent diet-D131, Augy, France) and filtered water in drinking bottles. The environment in housing, surgical facility, and procedural areas were maintained at 22 ± 3°C with a relative humidity between 30–70%. Twelve to 15 air changes/hour was maintained inside the animal room. The facility had an automated lighting which maintained a 12:12 h (0600 to 1800) light:dark photoperiodicity with a calibrated light intensity that was below 325 Lux at 1 meter height from the floor level inside the animal room. Rat tunnels (Citizen Industries, Ahmadabad, India) were provided inside the polysulphone cages for enrichment.

A qualified veterinarian performed the surgery using aseptic technique. Tracheostomy and thoracotomy were performed under anesthesia (ketamine hydrochloride, 80 mg/kg IM; xylazine hydrochloride, 10 mg/kg IM; 1.5% isoflurane) in 6 rats. The rats underwent ligation of the left anterior descending artery. The tracheostomy tube was placed by making a midventral neck incision and retracting the muscle tissue to expose the trachea; the tube was then connected to a small-animal ventilator (model R407, RWD Life Science, Guangdong, China) at 40 breaths per minute and 1.2 mL tidal volume per 100 g body weight. The sternum and the left costochondral junctions of the 2nd through 5th ribs were exposed. A left parasternal thoracotomy was performed by dissecting the pectoralis muscle, ribs at the costochondral junction, and pleura. Excess bleeding was prevented by cauterization. A retractor was placed between the 1st through 6th intercostal spaces at the sternal border and rib cage. The pericardium was grasped gently with an atraumatic forceps and incised to expose the heart. The left anterior descending artery was identified and ligated with a 7-0 Prolene suture (blue monofilament polypropylene nonabsorbable surgical suture USP, Centenial Surgical Suture, Maharashtra, India), sparing septal artery by keeping the angle of the atrial appendage as the landmark (Figure 1). The ensuing infarct region was identified by visible blanching and cyanosis immediately after ligation of the artery.

A lyophilized sterile sheet of C-ECM was cut to approximately 7 mm × 3 mm and grafted by suturing over the blanched area in 3 rats (test rats). The other 3 infarcted rats had no graft and formed the control group. A chest tube (luminal diameter, 2 mm) was placed, the chest retractor was removed, and the rib cage was

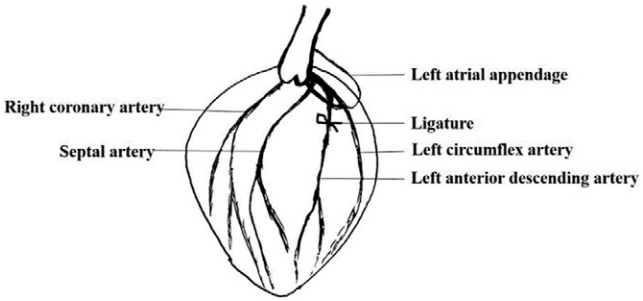

Figure 1. Diagram of rat heart (sternal view) showing the site of left coronary artery ligation made for inducing myocardial infarction.

apposed with the sternum. The muscle layer was sutured in place by using 3-0 Truglyde suture (Absorbable surgical suture USP, Centenial Sutures India). Then the skin was closed by using 3-0 Mersilk (nonabsorbable surgical suture USP, Ethicon, Raritan, NJ), air was suctioned from the thoracic cavity, and the chest tube was removed. The tracheostomy tube was removed after the rats regained spontaneous breathing. The rats were observed until a steady heart rate was attained, and they each received ceftriazone (20 mg/kg IM) and meloxicam (0.5 mg/kg IM) for 5 d. The rats were closely monitored for signs of discomfort.

Clinical monitoring. ***Estimation of serum cardiac biomarkers.*** Blood samples were collected from retro-orbital plexus of all rats for analysis of serum creatine phosphokinase, muscle–brain creatine kinase, and cardiac troponin T at 3 time points: 2 d before surgery (presurgery), 24 h after surgery (postsurgery), and 4 wk after surgery at the time of euthanasia (terminal).

ECG. Rats were anesthetized with 1.5% isoflurane in 100% oxygen. Three electrodes were placed on limbs (2 on forelimbs and one on a hindlimb), and at least 3 recordings were made (Biopac Student Lab, Biopac, Goleta, CA). The cardiac electrical activity was recorded at 1 and 4 wk after surgery and compared with the baseline values, which were recorded 1 d before the induction of MI. The following parameters were analyzed: heart rate, ST elevation, QT interval, QRS amplitude, QRS duration, RR amplitude and RR interval.

Echocardiography. Classic M-mode parasternal short-axis images were obtained by using a model HD11 XE ultrasound system (Philips, Newmarket, Ontario, Canada) before surgery and at 1 and 4 wk after surgery under ketamine hydrochloride (15 to 25 mg/kg) anesthesia. The measurements were done through the septum and left ventricular free wall. The following measurements were recorded: end-diastolic septum thickness, left ventricular end-diastolic internal diameter (LVIDd), left ventricular end-diastolic posterior wall thickness, end-systolic septum thickness, left ventricular internal dimension at end systole (LVIDs), and left ventricular posterior wall thickness at end systole.[26] Ejection fraction (EF) and fractional shortening (FS) were calculated by using the following equations:

$$EF = \frac{[(LVIDd)^3] - (LVIDs)^3]}{(LVIDd)^3} \times 100\%$$

$$FS = \frac{(LVIDd) - (LVIDs)}{(LVIDd)} \times 100\%$$

Necropsy and gross pathology. All rats were euthanized at 4 wk after the induction of MI. Gross lesions were evaluated, and tissue samples were fixed in 10% neutral buffered formalin for histomorphologic evaluation. Three transverse sections from lower side of the formalin-fixed hearts were used for histologic evaluation. Gross images were obtained and traced by using Photoshop (Adobe, San Jose, CA) to obtain representative drawings of the sections. *ImageJ* software was used for calibration and measurement of the total area of heart except for the 2 luminal areas and the infarct area. The area occupied by the scaffold

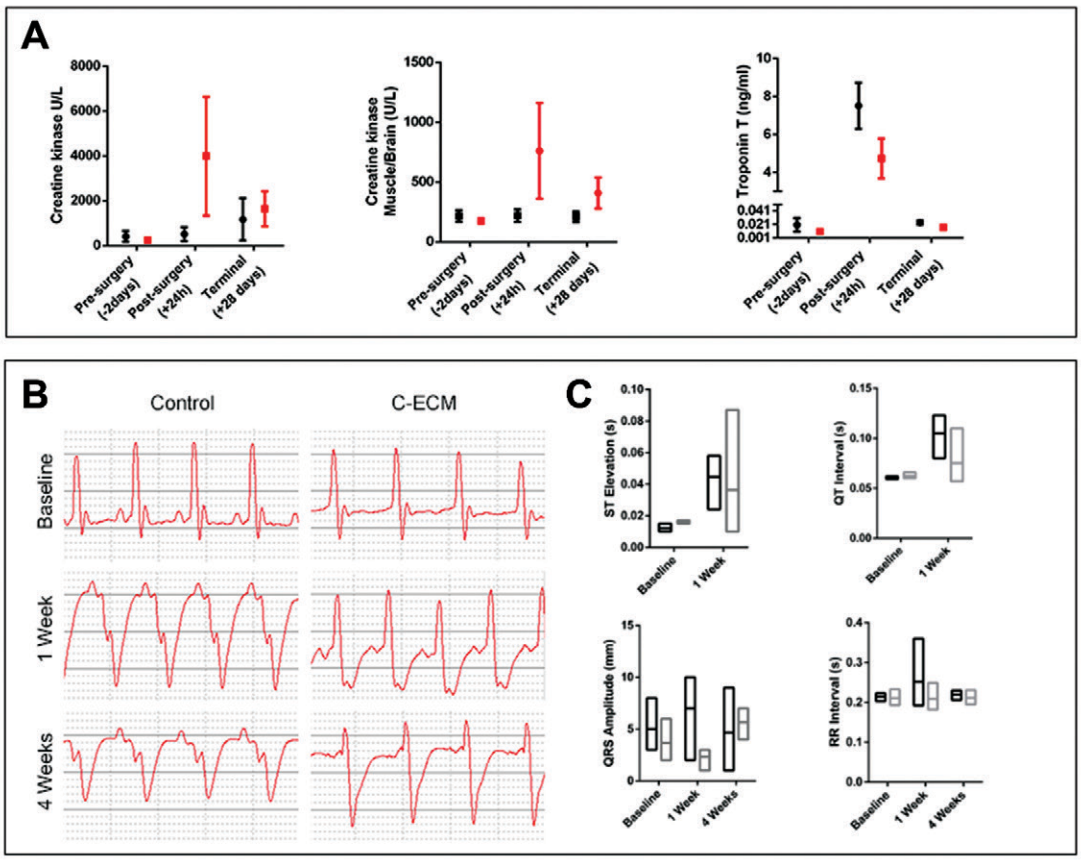

Figure 2. Clinical monitoring of myocardial infarction (MI) in rats. (A) Serum biochemical values of rats that underwent ligation of the left anterior descending coronary artery are significantly higher at 24 h after surgery than at baseline (−2 d), indicative of MI. Control, black; C-ECM, red. (B) Representative electrocardiograms of the control and C-ECM-grafted group recorded at baseline (−2 d) and at 1 and 4 wk after MI, indicating functional damage in the heart. (C) Box plot showing the ST elevation, QT interval, RR interval, and QRS amplitude of all rats in both groups, suggesting uniformity in the extent of MI between the 2 experimental groups (control, black; C-ECM, gray).

was omitted from the measurements. Then, the infarct area relative to the total cross-sectional area of heart was calculated and reported as a percentage.

Histology, immunohistochemistry, and morphometry. Tissue sections were processed by using an automated partially enclosed bench-top tissue processor (model TP1020, Leica Biosystems, Germany) and were embedded in paraffin. Tissue sections (thickness, 4 µm) were prepared by using a fully automated rotary microtome (model RM2255, Leica Biosystems). All histomorphologic and morphometric evaluations were completed under the direct supervision of a veterinary pathologist.

Histochemistry. Sections were stained routinely with Harris hematoxylin and eosin for histomorphology and with picrosirius red and Masson trichrome for collagen.[56] The area of infarction in all rats was calculated by using the trace tool of *ImagePro* (Media Cybernetics, Rockville, MD) on the sections stained with picrosirius red and Masson trichrome at 1.25× magnification. The fibrotic areas on Masson trichrome–stained sections at 40× magnification were quantified (30 images per rat) relative to the total area and reported as percentages. Herovici-stained sections were used to evaluate the differential distribution of type I and type III collagen.

Immunohistochemistry. Macrophages in the infarct region were detected by immunohistochemistry using CD68 antibody (dilution, 1:100; clone C68/684, catalog no. ab201340, Abcam, Cambridge, United Kingdom). The presence of mononuclear and proliferating cells near the biomaterial and in the infarct zone were detected by using antibodies against CD4 (1:100; clone MT310, catalog no. sc19641, Santa Cruz Biotechnology, Dallas, TX), CD8 (1:400; clone OX-8, catalog no. ab33786, Abcam), and proliferating cell nuclear antigen (PCNA; 1:400; clone PC10, catalog no. sc56, Santa Cruz Biotechnology). Angiogenesis at the infarct site was studied by using antibodies against α smooth muscle cell actin (1:300; clone B4, catalog. no. sc53142, Santa Cruz Biotechnology) and CD31 (1:400; clone PECAM1, catalog no. NB100-2284, Novus Biologicals, Englewood, CO). Myofibroblasts present in the reaction site were detected by an antibody to α smooth muscle cell actin (1:300; clone B4, catalog no. sc53142, Santa Cruz Biotechnology). Cell-to-cell connections were quantified by using an antibody against connexin 43 (1:200; clone CXN-6, catalog no. ab11369, Abcam). All of these reactions were detected by using the Supersensitive Polymeric–HRP detection system (Bio Genex Laboratories, Freemont, CA) and counterstaining with Harris hematoxylin. The images were captured by using a model DP71 camera loaded onto a model BX51 microscope (Olympus, Tokyo, Japan). All images were captured at 40× magnification.

Image analysis for histomorphometry. Histology images captured by using *ImagePro* software (version 3DS6.1, Media Cybernetics) were used for all counting and histomorphometric evaluations. The following parameters were studied on sections stained with hematoxylin and eosin: number of cells in the interventricular septum, length of longitudinally cut cardiomyocytes (Dmaj in µm), and diameter of those cardiomyocytes cut at cross-sectional planes (Dmin in µm).[8] From Masson trichrome–stained sections, we measured the areas of the right ventricular free wall, left ventricular free wall, and interventricular septum to confirm hypertrophy due to MI, represented by using a doughnut chart. In immunostained sections, *ImagePro* was used to quantify the number of positively stained cells and the vascular density at the infarct site.

Statistical analysis. Results are presented as mean ± SEM unless otherwise specified and analyzed by using PRISM 6.01 (GraphPad Software). The 2 groups were compared by using a 2-tailed Student *t* test. Two-way ANOVA was performed to analyze the serum values of troponin T, creatinine kinase, and myocardial:brain-specific creatine kinase. An α level of $P < 0.05$ was considered to indicate a significant difference between groups.

Results

Induction of MI and repair by grafting C-ECM. As compared with baseline values, serum concentrations of troponin T, creatine kinase and myocardial/brain specific creatine kinase were significantly higher (Figure 2 A) at 24 h after the ligation of the coronary artery in all rats (P = 0.0007 for the C-ECM

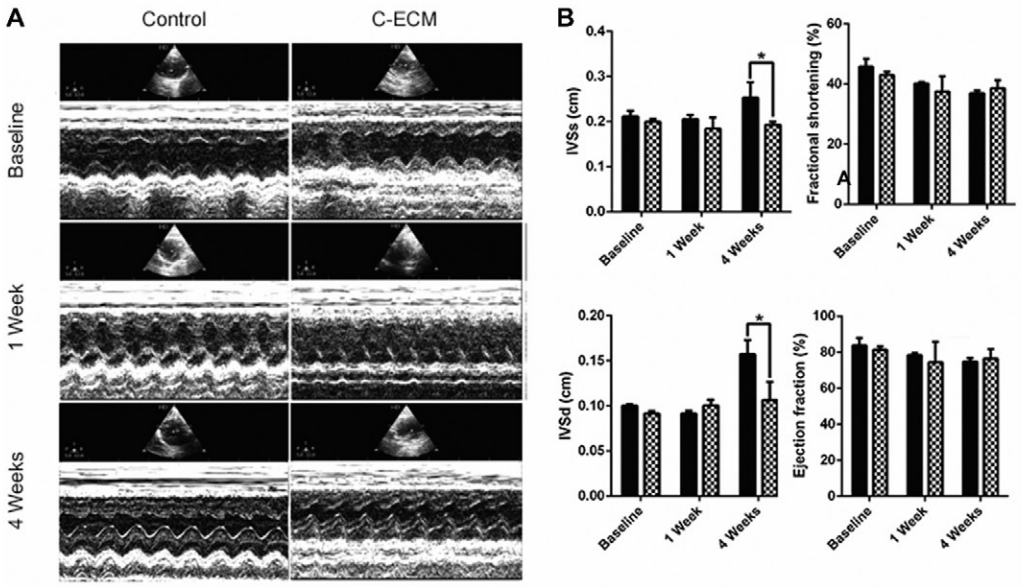

Figure 3. Echocardiographic monitoring of myocardial infarction (MI) in rats. (A) Representative echocardiographs of rats with MI. (B) Bar diagram showing the quantitative variation in the end-systolic septal thickness (IVSs), end-diastolic septal thickness (IVSd), and fractional shortening and ejection fraction at 1 and 4 wk, confirming the uniformity in the induction of MI between groups (control, solid bars; C-ECM, hatched bars). Data were analyzed by 2-way ANOVA followed by the Sidak multiple-comparisons test; *$P < 0.05$.

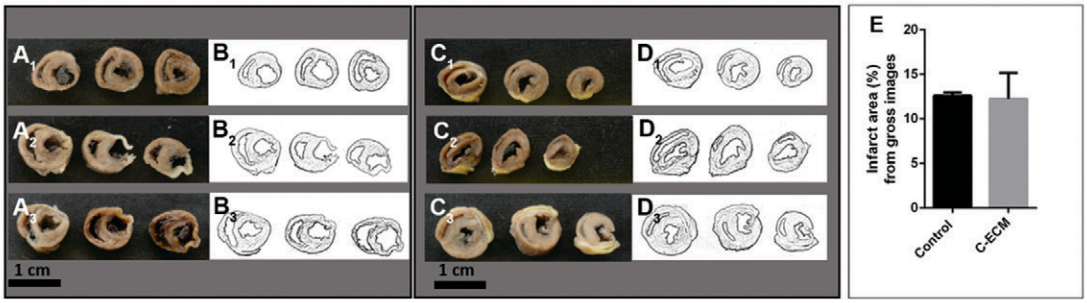

Figure 4. Confirmation of myocardial infarction (MI) based on necropsy. Gross photographs of cross sections of heart specimens of control rats (A_1–A_3) with their sketches (B_1–B_3) and rats with C-ECM–grafted hearts (C_1–C_3) with their sketches (D_1–D_3); samples were collected at necropsy, 4 wk after ligation of the left coronary artery. Samples show the extent of thinning and necrosis (appreciated as whitish areas) of the left ventricular free wall as well as differing degrees of concentric hypertrophy among rats. The subscripts 1–3 indicate cross-sections of the heart made at 3 planes posterior to the ligature. (E) The extent of the myocardial infarction was quantified and did not differ between groups.

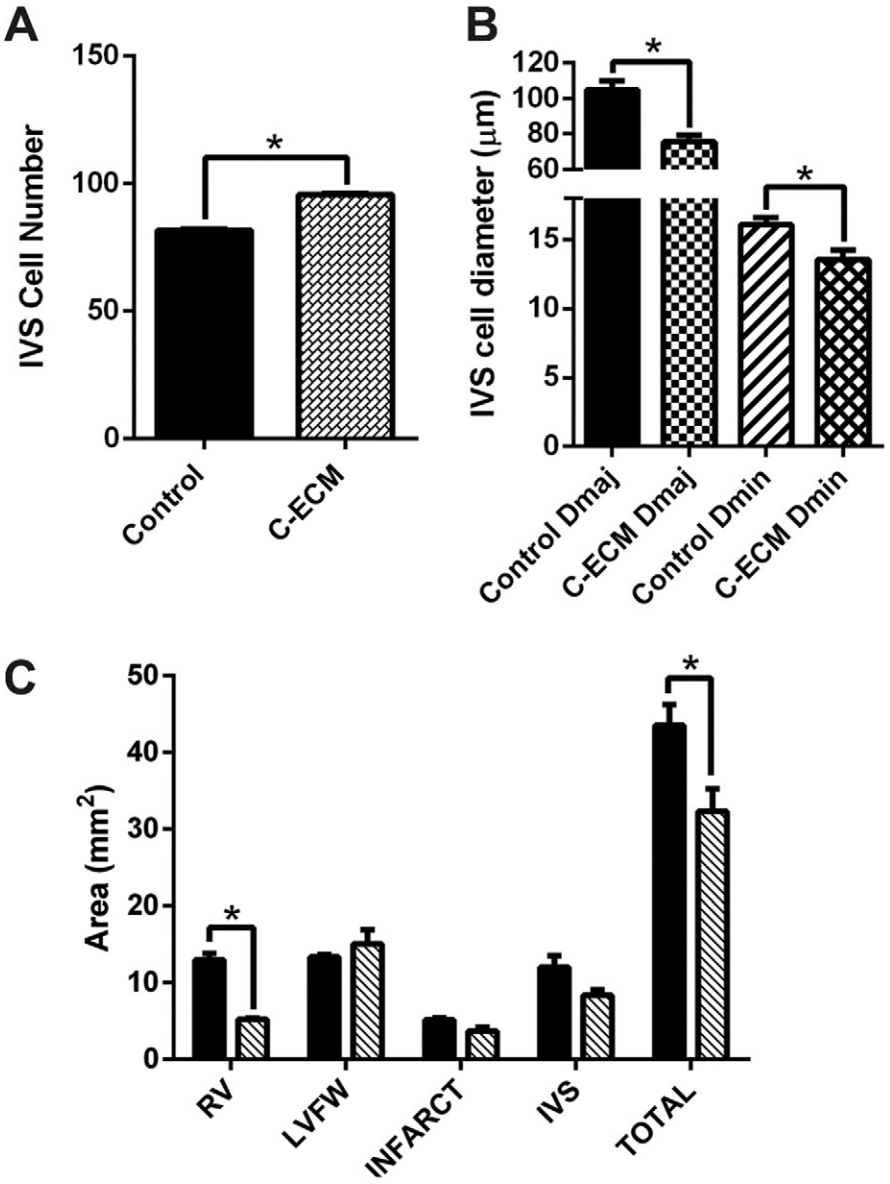

Figure 5. Quantification of histology images. Bar graph showing A, the number of myocardiocytes and B, their diameter (Dmaj, major cell diameter and Dmin, minor cell diameter) in the interventricular septum (IVS) counted from H&E images of control animals and cholecystic extracellular matrix (C-ECM)-grafted animals, $^*P < 0.05$ indicated significant difference between the groups. C, Bar graph showing the area of right ventricular (RV), left ventricular free wall (LVFW), infarct, interventricular septum (IVS) and the total area quantified from the Masson's trichrome stained images showing hypertrophy in the control group (control, solid bars; C-ECM, hatched bars).

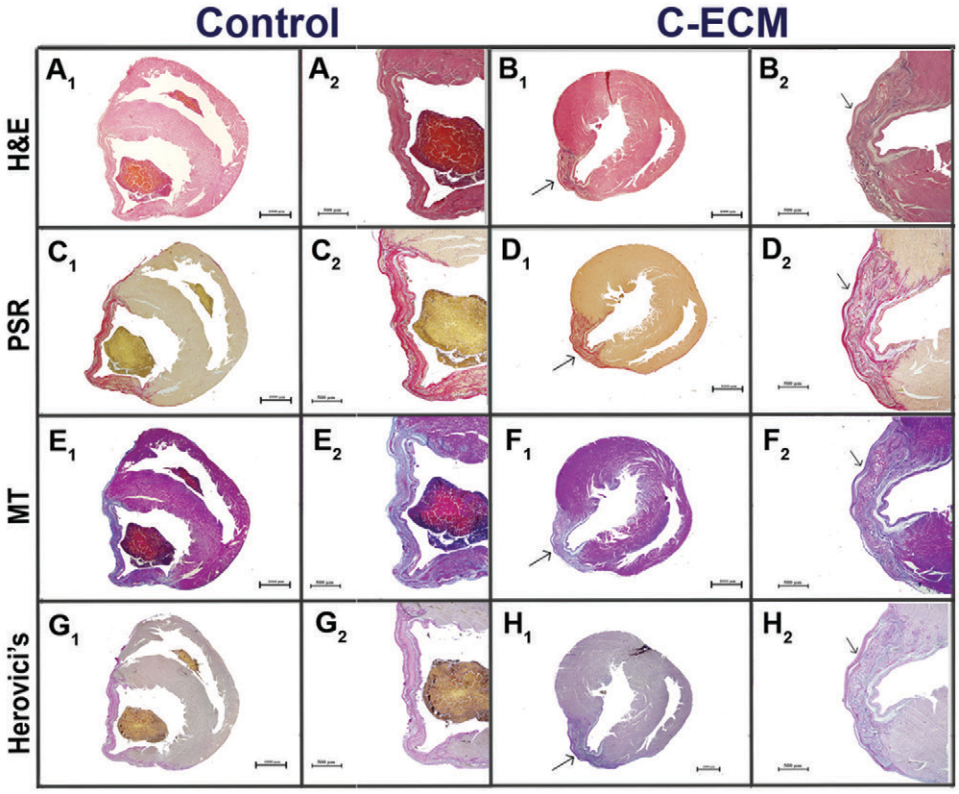

Figure 6. Histomorphologic evaluation of the heart (low magnification). Photomicrographs of representative histology sections stained with (A and B) hematoxylin and eosin (H&E), (C and D) picrosirius red (PSR), Masson trichrome (MT), and (G and H) Herovici stains of samples from the control rats (A, C, E, G) and C-ECM–grafted rats (B, D, F, H) at magnifications of 1.25× (subscript 1) and 4× (subscript 2). The extent of necrosis in these samples was evident at all magnifications, corroborating the observations at gross morphology (refer to Figure 8 for quantitative data). The grafted C-ECM (arrow) appeared as refractile material at the epicardial aspect of the myocardial wall. Note that panels A_2, C_2, E_2, and G_2 are stitched images, for improved illustration.

group and <0.0001 for the control group), indicating successful induction of MI.

Compared with baseline data, all ECGs (Figure 2 B and C) recorded from all rats at 1 and 4 wk after the surgery had deviations from normal. The echocardiograms showed narrowing of the differences in the end-systolic and end-diastolic septal thicknesses between groups at 4 wk, indicating possible recovery from the infarct in the C-ECM–grafted group (Figure 3 A and B). At 4 wk, fractional shortening and the ejection fraction of the C-ECM–grafted rats were near baseline values (Figure 3 B).

Gross pathology and histopathology. Gross signs of necrosis, mural thinning, and interventricular septal hypertrophy (Figure 4 and 5) were present in both groups, as expected during healing after MI. No difference in the proportion of MI-affected tissue was apparent between the groups on visual examination or by stereology (Figure 4 E). However, the graft appeared to have integrated with the heart (Figure 4 C_1 through C_3).

The sections stained with hematoxylin and eosin showed the extent of left ventricular myocardial degeneration or necrosis and replacement fibrosis after MI (Figure 6 A_1, A_2, B_1, and B_2, and Figure 7 A and B). Both groups showed MI-induced thinning of the left ventricular wall. Picrosirius red staining differentiated collagen (red) from muscle tissue (yellow) (Figures 6 C and D and 7 C and D). Because it was collagen-rich, the C-ECM graft also stained red. The necrotic region in the left ventricular region was well distinguished by this staining, as evident from the compact collagen fibers (Figure 6 C_1, C_2, D_1, and D_2). Staining with Masson trichrome corroborated the findings; collagen-rich necrotic fibrous tissue was stained blue (Figures 6 E_1, E_2, F_1, and F_2 and 7 E and F). The higher-magnification images of the Masson trichrome–stained sections showed a difference in collagen compactness between the groups (Figure 7 E and F). As expected, the C-ECM graft also stained blue because of its abundant collagen.[7] Left ventricular thinning was prominent, but the extent of infarction was not different between the 2 groups (Figure 8 A and B).

We used histomorphometry to quantify the area occupied by total collagen and found that it was significantly ($P < 0.05$) lower in the C-ECM–grafted rats than in the control group (Figure 8 C). This difference was further investigated by using Herovici polychromatic stain for type I and type III collagen, which stained pink and blue respectively (Figures 6 G_1, G_2, H_1, and H_2 and 7 G and H). The remodeling reaction after MI in the C-ECM group was largely due to type III collagen rather than type I collagen (Figure 8 D and E). The type I:type III collagen ratio was 2.4 ± 0.5 in the control group and 1.8 ± 0.4 after C-ECM–graft-assisted healing; these values were not significantly different.

Immunohistochemistry. At 4 wk after MI, obvious chronic inflammation with predominantly mononuclear cell infiltration was present in all tissue sections studied. The distribution of macrophages in necrotic tissue was similar in both groups of rats (Figure 9 A_2, B_2, and C_2). Occasionally giant cells were present near the grafts (Figure 9 B_2), but the biomaterial appeared to have induced a different inflammatory reaction with prominent infiltration of mononuclear cells (Figure 9 B_3 and B_4, Figure 10)

Connexin 43, a gap-junction protein of the intercalated disk responsible for maintaining electrical conductivity, was detected by immunostaining. The staining facilitated the detection of functional cardiomyocytes. No positive cells were found in the infarct area, but the non-infarcted area had many positive

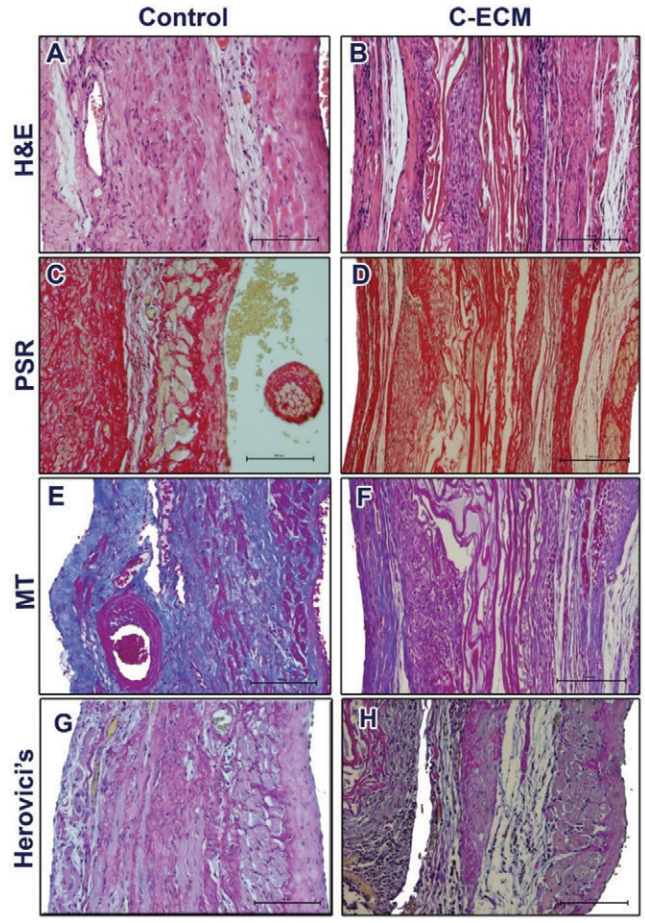

Figure 7. Histomorphologic evaluation of the heart (high magnification). Photomicrographs of representative histology sections stained with (A and B) hematoxylin and eosin (H&E), (C and D) picrosirius red (PSR), (E and F) Masson trichrome (MT), and (G and H) Herovici stains of samples from the control rats (A, C, E, and G) and C-ECM-grafted rats (B, D, F, H); magnification, 40×. Myocardial degeneration and necrosis, moderate chronic inflammation, and moderate fibrosis were apparent at higher magnifications. Note that panels A, B, C, D, and F are stitched images, for improved illustration.

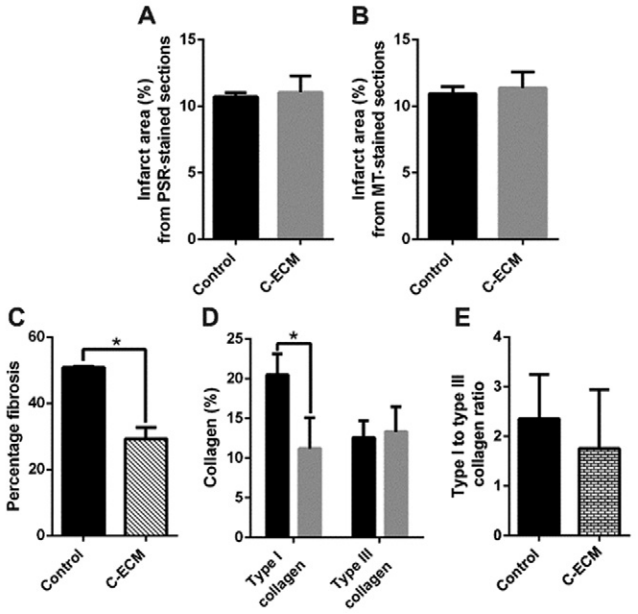

Figure 8. Quantification of infarct area and collagen deposition. Bar diagram representing stereology data **A)** the proportion of the infarct area, estimated by image analysis from images of tissue sections stained with (A) picrosirius red (PSR) and (B) Masson trichrome (MT). Infarct area was not different between groups, further indicating the uniformity in MI induction across the 2 experimental groups. Bar graphs showing significant (*$P < 0.05$; unpaired *t*-test) reduction in the (C) percentage of fibrosis in the presence of the C-ECM graft and in the (D) percentage area occupied by type I collagen and type III collagen, indicating a significant (*$P < 0.05$; unpaired *t*-test) decrease in the type I collagen content in the C-ECM group (control, black; C-ECM, gray). (E) Bar graph showing the ratio of type I to III collagen in the control group compared with the C-ECM group.

cells (Figure 11). Immunohistochemistry for PCNA showed proliferating cells in the infarct region containing the scaffold. As expected, cell proliferation was absent in the infarcted myocardium in both groups (Figure 9 A_1). However, many cells infiltrating around the graft had proliferative potential (Figure 9 B_1 and C_1, Figure 12).

Immunohistochemistry for macrophages and lymphocytes revealed differences in the nature of the chronic inflammation between groups. More CD4 lymphocytes were present (*p* value 0.0465) around the grafted biomaterial (36 ± 6 cells per high-power field) as compared with the control (18 ± 2 cells per high-power field). More specifically, C-ECM–grafted rats had a higher CD4:CD8 ratio (*p* value 0.0692) (Figure 13), indicating acceptance of the graft.

Immunohistochemistry for CD31 (a vascular endothelial cell marker) revealed sprouts of budding capillaries (Figure 14 A_1 and A_2), and a smooth muscle marker for actin showed well-differentiated leomyocytes (Figure 14 B_1 and B_2) in the tunica media; these cells are considered an indication of the functionality of newly formed blood vessels.[14,53] Sprouting capillaries and functional blood vessels were more abundant in the infarct area of the C-ECM–grafted rats as compared with the control rats ($P = 0.021$ and 0.008, respectively) (Figure 14 A_3 and B_3).

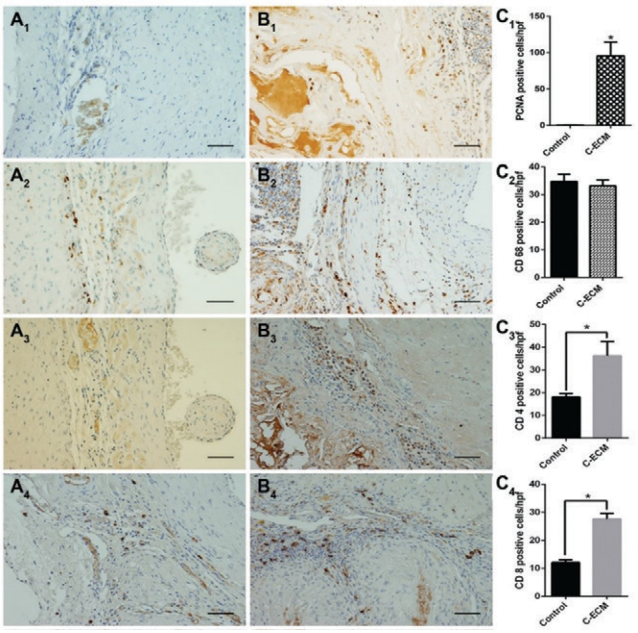

Figure 9. Immunohistochemistry for specific proteins. Light micrographs of histology sections collected from (A) control and (B) C-ECM–grafted rats after immunostaining with antibodies against proliferating cell nuclear antigen (PCNA; subscript 1), CD68 (macrophages; 2), CD4 (helper T-lymphocytes; 3), and CD8 (cytotoxic T-lymphocytes; 4). Scale bars, 50 µm. (C) Bar diagrams showing the quantitative information of the positive cells in these 2 groups. *$P < 0.05$ (unpaired *t*-test).

Discussion

This study investigated the healing effects of an epicardial graft that had been made of an adequately characterized C-ECM prepared by using a nondetergent and nonenzymatic method[3,33] in a rat coronary artery ligation model of MI. In this model, surgical ligation of the left anterior descending coronary artery induced a varying area of MI depending on the tightness of the ligature.[23] In the present study, ligation resulted in MI in all rats, as evidenced by serum biochemistry (Figure 2 A), ECG (Figure 2 B and C), and echocardiography (Figure 3 A and B), with no deaths. By 24 h after surgery (Figure 2 A), the level of cardiac troponin T, a marker of myocardial injury, had increased 400-fold in both groups. Serum levels of creatine kinase and myocardial–brain-specific creatine kinase were also increased above baseline (Figure 2 A), as is expected during MI.[38] The depression in the ST segment of the ECG (Figure 2B, C) indicated the persistence of MI in all of the experimental rats, even at 1 wk after surgery. However, the echocardiographs (Figure 3 A and B) of the 2 groups were not significantly different during the ejection fraction and fractional shortening, thus indicating similar functional damage to the heart. The changes were present for up to 4 wk after the induction of MI. The extent of tissue necrosis was similar in the test and control groups. The gross pathologic (Figure 4) and histomorphologic findings showed the extent of MI and the nature

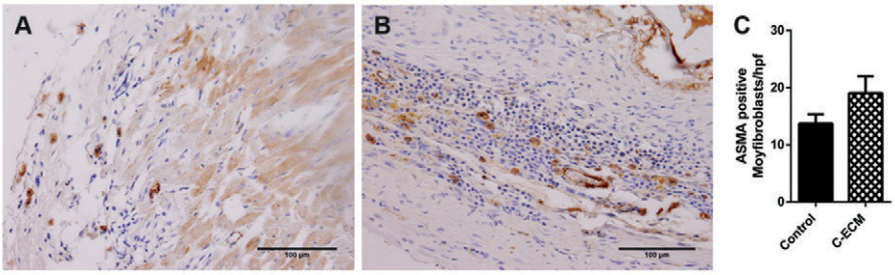

Figure 10. Immunohistochemistry for myofibroblasts. A, Light micrographs of histology sections collected from control and B, cholecystic extracellular matrix (C-ECM)-grafted animals after immunostaining for α-smooth muscle actin (ASMA) positive myofibroblasts, confirming similar fibrogenesis in both the groups as evident from C, the representative graph indicating no difference between the groups. Scale bar, 100 µm.

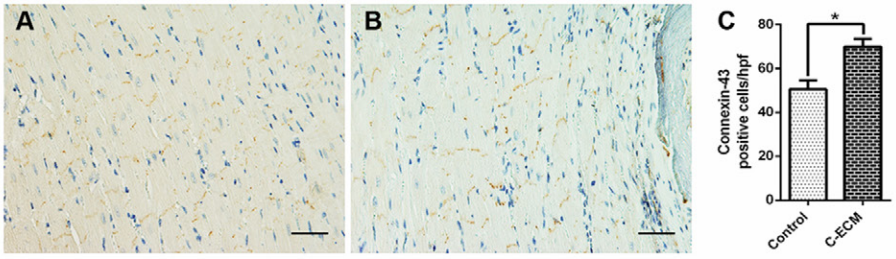

Figure 11. Expression of Connexin 43. Photomicrographs showing the difference in the number of Connexin 43 cells demonstrated by immunohistochemistry to CN43 epitope, in A, control B, C-ECM group and C, bar graph showing the quantitative data (scale bar, 50 µm). The results were analysed by unpaired *t*-test (*$P < 0.05$).

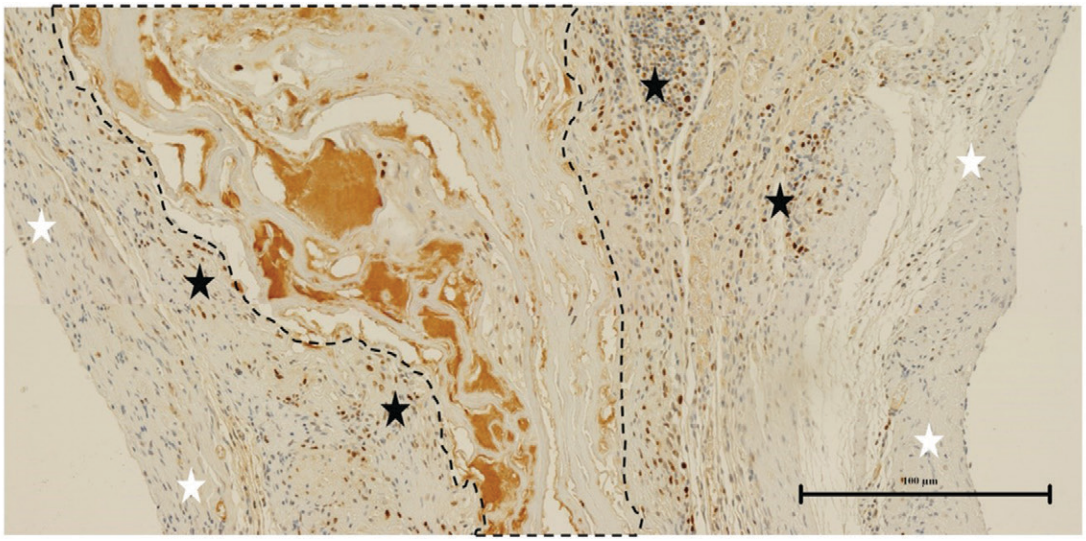

Figure 12. Differential distribution of proliferating cells proximal and distal the xenograft. Light micrograph of a cholecystic extracellular matrix (C-ECM, lakes of brown coloured biomaterial, marked by black dotted lines) graft-assisted healing reaction in myocardium following myocardial infarction demonstrating the abundance of proliferating cell nuclear antigen (PCNA) positive brown coloured nucleated cells proximal (black asterisk) compared to distal (white asterisk) areas of the infarct. (* a composite of 8 stitched images is presented for better illustration) Scale bar, 100 µm. Please see the Fig. 9 C_1 for the quantitative data.

of healing reaction in both groups (Figures 6 and 7), but with measurable differences in tissue remodeling reaction between groups. Several histomorphometric features (Figures 6 to 10) revealed the differential nature of the tissue remodeling reaction, with stronger remodeling and regenerative reactions in rats with C-ECM grafts as compared with the control group.

In general, tissue remodeling in most injured tissues is characterized by a regenerative response in the parenchyma and a reparative process in the connective tissue.[22] However, the myocardial parenchyma may not mount a significant regenerative response (Figure 9 A_1) due to the G_0 status of highly differentiated myocardiocytes.[55] This dampened response is in part responsible for the fibrotic scarring associated with tissue remodeling after cardiac injury. Therefore, in the present study, the data suggest that the C-ECM graft stimulated a tissue-remodeling and regenerative reaction based on results of the immunohistochemistry for connexin 43 (Figures 11). The more numerous connexin 43–positive cells near the infarct in the test group as compared with the controls suggest the preservation of cell-to-cell connection (Figure 11 A to C).

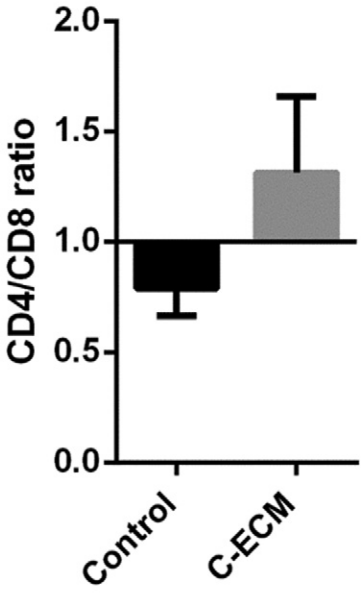

Figure 13. Anti-inflammatory response of lymphocytes to the xenograft. A pictogram representing the ratio of CD4 (helper T lymphocytes) to CD8 (cytotoxic T lymphocytes) positive cells in the infarct areas of both the groups, deducted from the data presented in Fig. 9: A3-C3, A4-C4. The ratio was higher in the C-ECM group indicating an anti-inflammatory graft acceptance reaction compared to a pro-inflammatory reaction in unassisted healing response.

The recruitment of extramyocardial cells to the defect site is one of the major mechanisms by which ECM-based biomaterials promote healing in a myocardial infarct.[13,32] In the present study, the immunohistochemistry for PCNA (Figure 9 B_1) showed the presence of significantly higher numbers of proliferating cells in the myocardium grafted with C-ECM as compared with the control rats. We did not identify these cells, but they are not native to the heart, given that native myocardial cells have limited proliferative potential.[55] At least some of these PCNA-immunoreactive cells could be sprouting blood vessels.[29]

Restoration of blood circulation to the infarcted myocardium is a major therapeutic goal. Although we did not attempt interventional cardiology in the present study, histomorphology revealed excellent angiogenesis in the damaged heart tissue in rats grafted with C-ECM compared with rats lacking grafts (Figure 14 A_1 through A_3 and B_1 through B_3). The extent of oxygenation or reperfusion could not be evaluated histologically in the MI region; however, the morphometric data suggested the possibility of differential reperfusion between groups. The graft clearly promoted the recruitment of cells that participated in angiogenesis at the MI site.

The infiltration of mononuclear cells can be expected in any healing reaction, especially those around tissue grafts.[28,50] However, in the present experiment, the graft did not induce a classic foreign body granulomatous inflammation predominated by macrophages. In contrast, the number of macrophages, as demonstrated by immunohistochemistry for CD68, (Figure 9 A_2, B_2, and C_2), was much lower than the numbers of infiltrating CD4 (helper T cells) and CD8 (cytotoxic T cells) lymphocytes (Figure 9 C_3 and C_4). This finding indicates the presence of a tissue remodeling reaction.[12]

Cardiac injury of any type results in fibrotic scarring, either through replacement fibrosis or interstitial fibrosis.[43]

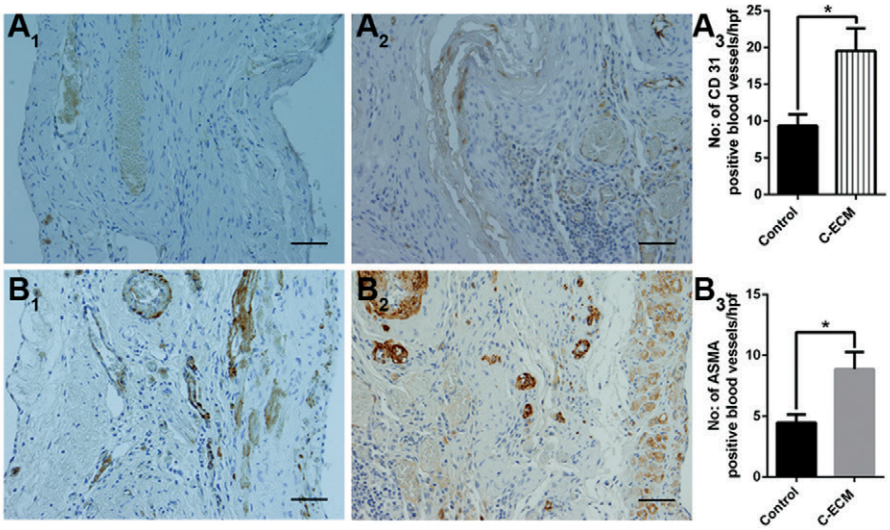

Figure 14. Immunohistochemistry for CD31 and ASMA. Light micrographs of histology sections collected from (A) control and (B) C-ECM–grafted rats after immunostaining with antibodies against CD31 and α smooth muscle actin (ASMA); scale bar, 50 μm. (C) Bar diagrams showing the quantitative information of the positive cells in these 2 groups. *$P < 0.05$ (unpaired t-test).

The differential nature of the fibrotic reaction between groups was seen in the results of the immunohistochemistry for myofibroblasts (Figure 10) and histochemistry for collagen (picrosirius red, Figures 6 C and D and 7 C and D; Masson's trichrome, Figures 6 E and F and 7 E and F; and Herovici, Figures 6 G and H and 7 G and H). In the sections stained with picrosirius red, the area occupied by collagen was reduced in the C-ECM–grafted rats. Moreover, the high-magnification trichrome images showed that the nature of the fibrotic reaction in the C-ECM–grafted rats was remarkably different from that of nongrafted rats. The fibrosis in the grafted rats was more of an interstitial type, whereas the control group had a replacement type of fibrosis. Myofibroblasts are known to synthesize at least 2 subtypes of collagen, type I and type III.[44] Type I collagen is essentially composed of highly crosslinked fibrillar collagen that is relatively insensitive to enzymatic degradation, compared with the reticular type III collagen, which is amenable to degradation.[52] Both collagen types are present in all tissues and healing wounds, but the relative proportion defines elasticity and the nature of the regenerative response.[60] Terminally matured inelastic scar has abundance of type I collagen in proportion to type III collagen.[17]

In the present experiment, type III collagen was more abundant than type I (Figure 8 D), indicating that the presence of C-ECM had prevented or delayed the formation of type I collagen. Given that no currently available synthetic or natural biomaterial is known to reverse cardiac fibrosis, the observation that the C-ECM mitigated the deposition of type I collagen is noteworthy. In human cardiac tissue, the ratio of type I to type III collagen is 8 to 1 and in normal rat cardiac tissue is 2.2 to 1.5,[64] and the ratio changes due to a progressive fibrotic reaction associated with tissue injury or old age.[19] However, the ratio associated with C-ECM–graft-assisted healing was 1.75, due to the higher type III collagen content. This finding reflects reduced or delayed deposition of type I collagen. In a previous study, higher expression of type III collagen improved heart function in left ventricular remodeling after MI.[61] The current study included only 3 rats in each group. Using more rats, euthanizing them at more frequent intervals, and demonstrating MI grossly by using appropriate stains may have clarified these points, especially the dynamics of collagen deposition. We consider these drawbacks to be major limitations of the current study. Nevertheless, our results strongly indicate that using C-ECM mitigated the nature of fibrotic scarring after MI.

As clinicians strive for strategies to mitigate cardiac fibrosis in human patients, the use of C-ECM as an epicardial graft offers a credible treatment option. Delayed fibrosis extends the period for clinicians to identify and deploy appropriate therapeutic strategies for managing scarring. Here, we applied biomaterial as a thin sheet; this form may be unsuitable for human cardiovascular therapy, given that thoracotomy soon after MI may not be appropriate. Nevertheless, the demonstrated ability of the biomaterial to mitigate replacement fibrosis supports the development of alternative approaches (e.g., injectable gel) for delivering C-ECM, with the help of contemporary interventional cardiology tools, in order to optimize the use of this biomaterial in patients. Future investigations will help to unravel the cellular and molecular mechanisms responsible for delayed scarring and the pathobiology of cardiac remodeling.

Acknowledgments

RSN acknowledges the support from Department of Science and Technology, Government of India (INSPIRE fellowship grant no. IF 140709). PKS acknowledges the support from the Science and Engineering Research Board of India (grant no. SB/S2/RJN-152/2014). RSN thanks Dr Geetha C Surendran, Mr Kanakarajan V Pratheesh, Ms Manjula P Mony, and Ms Reshmi Raj for their help in performing animal experiments. All animal experiments were completed after prior approval from the Institutional Animal Ethics Committee and in accordance with approved institutional protocol (SCT/IAEC-198/NOVEMBER/2016/90).

References

1. **Aamodt JM, Grainger DW.** 2016. Extracellular matrix-based biomaterial scaffolds and the host response. Biomaterials **86**:68–82. https://doi.org/10.1016/j.biomaterials.2016.02.003.
2. **Anderson JL, Morrow DA.** 2017. Acute myocardial infarction. N Engl J Med **376**:2053–2064. https://doi.org/10.1056/NEJMra1606915
3. **Anilkumar TV, Vineetha VP, Revi D, Muhamed J, Rajan A.** 2014. Biomaterial properties of cholecyst-derived scaffold recovered by a nondetergent–enzymatic method. J Biomed Mater Res B Appl Biomater **102**:1506–1516. https://doi.org/10.1002/jbm.b.33131.
4. **Azevedo PS, Polegato BF, Minicucci MF, Paiva SAR, Zornoff LAM.** 2016. Cardiac remodeling: Concepts, clinical impact, pathophysiological mechanisms, and pharmacologic treatment. Arq Bras Cardiol **106**:62–69. https://doi.org/10.5935/abc.20160005.
5. **Balakrishnan-Nair DK, Nair ND, Venugopal SK, Das VN, George S, Abraham MJ, Eassow S, Alison MR, Sainulabdeen A, Anilkumar TV.** 2018. An immunopathological evaluation of the porcine cholecyst matrix as a muscle repair graft in a male rat abdominal wall defect model. Toxicol Pathol **46**:169–183. https://doi.org/10.1177/0192623317752894.
6. **Behfar A, Crespo-Diaz R, Terzic A, Gersh BJ.** 2014. Cell therapy for cardiac repair—lessons from clinical trials. Nat Rev Cardiol **11**:232–246. https://doi.org/10.1038/nrcardio.2014.9.
7. **Burugapalli K, Thapasimuttu A, Chan JCY, Yao L, Brody S, Kelly JL, Pandit A.** 2007. Scaffold with a natural mesh-like architecture: Isolation, structural, and in vitro characterization. Biomacromolecules **8**:928–936. https://doi.org/10.1021/bm061088x.
8. **Coelho-Filho OR, Shah RV, Mitchell R, Neilan TG, Moreno H, Simonson B, Kwong R, Rosenzweig A, Das S, Jerosch-Herold M.** 2013. Quantification of cardiomyocyte hypertrophy by cardiac magnetic resonance: Implications for early cardiac remodeling. Circulation **128**:1225–1233. https://doi.org/10.1161/CIRCULATIONAHA.112.000438.
9. **Cui Z, Yang B, Li RK.** 2016. Application of biomaterials in cardiac repair and regeneration. Engineering **2**:141–148. https://doi.org/10.1016/J.ENG.2016.01.028.
10. **Fanaroff AC, Morrow V, Krucoff MW, Seltzer JH, Perin EC, Taylor DA, Miller LW, Zeiher AM, Fernández-Avilés F, Losordo DW, Henry TD, Povsic TJ.** 2018. A path forward for regenerative medicine. Circ Res **123**:495–505. https://doi.org/10.1161/CIRCRESAHA.118.313261.
11. **Fernández-Pérez J, Ahearne M.** 2019. The impact of decellularization methods on extracellular matrix–derived hydrogels. Sci Rep **9**:14933. https://doi.org/10.1038/s41598-019-49575-2.
12. **Frangogiannis NG.** 2012. Regulation of the inflammatory response in cardiac repair. Circ Res **110**:159–173. https://doi.org/10.1161/CIRCRESAHA.111.243162.
13. **Frangogiannis NG.** 2017. The extracellular matrix in myocardial injury, repair, and remodeling. J Clin Invest **127**:1600–1612. https://doi.org/10.1172/JCI87491.
14. **Goncharov NV, Popova PI, Avdonin PP, Kudryavtsev IV, Serebryakova MK, Korf EA, Avdonin PV.** 2020. Markers of Endothelial Cells in Normal and Pathological Conditions. Biochem (Mosc) Suppl Ser A Membr Cell Biol **14**:167. https://doi.org/10.1134/S1990747819030140.
15. **Hashimoto H, Olson EN, Bassel-Duby R.** 2018. Therapeutic approaches for cardiac regeneration and repair. Nat Rev Cardiol **15**:585–600. https://doi.org/10.1038/s41569-018-0036-6.
16. **Hastings CL, Roche ET, Ruiz-Hernandez E, Schenke-Layland K, Walsh CJ, Duffy GP.** 2015. Drug and cell delivery for cardiac regeneration. Adv Drug Deliv Rev **84**:85–106. https://doi.org/10.1016/j.addr.2014.08.006.

17. **Hinderer S, Schenke-Layland K.** 2019. Cardiac fibrosis: A short review of causes and therapeutic strategies. Adv Drug Deliv Rev **146**:77–82. https://doi.org/10.1016/j.addr.2019.05.011.
18. **Horejs CM, St-Pierre JP, Ojala JRM, Steele JAM, Da Silva PB, Rynne-Vidal A, Maynard SA, Hansel CS, Rodríguez-Fernández C, Mazo MM, You AYF, Wang AJ, von Erlach T, Tryggvason K, López-Cabrera M, Stevens MM.** 2017. Preventing tissue fibrosis by local biomaterials interfacing of specific cryptic extracellular matrix information. Nat Commun **8**:15509. https://doi.org/10.1038/ncomms15509.
19. **Horn MA, Trafford AW.** 2016. Aging and the cardiac collagen matrix: Novel mediators of fibrotic remodelling. J Mol Cell Cardiol **93**:175–185. https://doi.org/10.1016/j.yjmcc.2015.11.005.
20. **Huang K, Ozpinar EW, Su T, Tang J, Shen D, Qiao L, Hu S, Li Z, Liang H, Mathews K, Scharf V, Freytes DO, Cheng K.** 2020. An off-the-shelf artificial cardiac patch improves cardiac repair after myocardial infarction in rats and pigs. Sci Transl Med **12**:9683. https://doi.org/10.1126/scitranslmed.aat9683.
21. **Huang S, Frangogiannis NG.** 2018. Antiinflammatory therapies in myocardial infarction: Failures, hopes, and challenges. Br J Pharmacol **175**:1377–1400. https://doi.org/10.1111/bph.14155.
22. **Iismaa SE, Kaidonis X, Nicks AM, Bogush N, Kikuchi K, Naqvi N, Harvey RP, Husain A, Graham RM.** 2018. Comparative regenerative mechanisms across different mammalian tissues. NPJ Regen Med **3**:6. https://doi.org/10.1038/s41536-018-0044-5.
23. **Kainuma S, Miyagawa S, Fukushima S, Tsuchimochi H, Sonobe T, Fujii Y, Pearson JT, Saito A, Harada A, Toda K, Shirai M, Sawa Y.** 2017. Influence of coronary architecture on the variability in myocardial infarction induced by coronary ligation in rats. PLoS One **12**:e0183323. https://doi.org/10.1371/journal.pone.0183323.
24. **Karthika S, Anoop S, Devanand CB, Narayanan MK, Unni M, Eassow S, Anilkumar T.** 2018. A porcine-cholecyst-derived scaffold for treating full thickness lacerated skin wounds in dogs. Vet Res Commun **42**:233–242. https://doi.org/10.1007/s11259-018-9731-3.
25. **Kc P, Hong Y, Zhang G.** 2019. Cardiac tissue-derived extracellular matrix scaffolds for myocardial repair: Advantages and challenges. Regen Biomater **6**:185–199. https://doi.org/10.1093/rb/rbz017.
26. **Kumar V, Aneesh Kumar A, Sanawar R, Jaleel A, Santhosh Kumar TR, Kartha CC.** 2019. Chronic pressure overload results in deficiency of mitochondrial membrane transporter ABCB7 which contributes to iron overload, mitochondrial dysfunction, metabolic shift and worsens cardiac function. Sci Rep **9**:13170. https://doi.org/10.1038/s41598-019-49666-0.
27. **Liu B, Lee BW, Nakanishi K, Villasante A, Williamson R, Metz J, Kim J, Kanai M, Bi L, Brown K, Di Paolo G, Homma S, Sims PA, Topkara VK, Vunjak-Novakovic G.** 2018. Cardiac recovery via extended cell-free delivery of extracellular vesicles secreted by cardiomyocytes derived from induced pluripotent stem cells. Nat Biomed Eng **2**:293–303. https://doi.org/10.1038/s41551-018-0229-7.
28. **Ma Y, Mouton AJ, Lindsey ML.** 2018. Cardiac macrophage biology in the steady-state heart, the aging heart, and following myocardial infarction. Transl Res **191**:15–28. https://doi.org/10.1016/j.trsl.2017.10.001.
29. **Marín-Juez R, Marass M, Gauvrit S, Rossi A, Lai SL, Materna SC, Black BL, Stainier DYR.** 2016. Fast revascularization of the injured area is essential to support zebrafish heart regeneration. Proc Natl Acad Sci USA **113**:11237–11242. https://doi.org/10.1073/pnas.1605431113.
30. **Mewhort HEM, Svystonyuk DA, Turnbull JD, Teng G, Belke DD, Guzzardi DG, Park DS, Kang S, Hollenberg MD, Fedak PWM.** 2017. Bioactive extracellular matrix scaffold promotes adaptive cardiac remodeling and repair. JACC Basic Transl Sci **2**:450–464. https://doi.org/10.1016/j.jacbts.2017.05.005.
31. **Mewhort HEM, Turnbull JD, Meijndert HC, Ngu JMC, Fedak PWM.** 2014. Epicardial infarct repair with basic fibroblast growth factor–enhanced CorMatrix-ECM biomaterial attenuates postischemic cardiac remodeling. J Thorac Cardiovasc Surg **147**:1650–1659. https://doi.org/10.1016/j.jtcvs.2013.08.005.
32. **Mewhort HEM, Turnbull JD, Satriano A, Chow K, Flewitt JA, Andrei AC, Guzzardi DG, Svystonyuk DA, White JA, Fedak PWM.** 2016. Epicardial infarct repair with bioinductive extracellular matrix promotes vasculogenesis and myocardial recovery. J Heart Lung Transplant **35**:661–670. https://doi.org/10.1016/j.healun.2016.01.012.
33. **Mony MP, Anilkumar TV.** 2020. Controlled cross-linking of porcine cholecyst extracellular matrix for preparing tissue engineering scaffold. J Biomed Mater Res B Appl Biomater **108**:1057–1067. https://doi.org/10.1002/jbm.b.34457.
34. **Mony MP, Shenoy SJ, Raj R, Geetha CS, Pratheesh KV, Nair RS, Purnima C, Anilkumar TV.** 2021. Gelatin-modified cholecyst-derived scaffold promotes angiogenesis and faster healing of diabetic wounds. ACS Appl Bio Mater **4**:3320–3331. https://doi.org/10.1021/acsabm.0c01648.
35. **Muhamed J, Rajan A, Surendran A, Jaleel A, Anilkumar TV.** 2017. Comparative profiling of extractable proteins in extracellular matrices of porcine cholecyst and jejunum intended for preparation of tissue engineering scaffolds. J Biomed Mater Res B Appl Biomater **105**:489–496. https://doi.org/10.1002/jbm.b.33567.
36. **Muhamed J, Revi D, Rajan A, Anilkumar TV.** 2015. Comparative local immunogenic potential of scaffolds prepared from porcine cholecyst, jejunum, and urinary bladder in rat subcutaneous model. J Biomed Mater Res B Appl Biomater **103**:1302–1311. https://doi.org/10.1002/jbm.b.33296.
37. **Muhamed J, Revi D, Rajan A, Geetha S, Anilkumar TV.** 2015. Biocompatibility and immunophenotypic characterization of a porcine cholecyst–derived scaffold implanted in rats. Toxicol Pathol **43**:536–545. https://doi.org/10.1177/0192623314550722.
38. **Mythili S, Malathi N.** 2015. Diagnostic markers of acute myocardial infarction. Biomed Rep **3**:743–748. https://doi.org/10.3892/br.2015.500.
39. **Nair RS, Ameer JM, Alison MR, Anilkumar TV.** 2017. A gold nanoparticle coated porcine cholecyst-derived bioscaffold for cardiac tissue engineering. Colloids Surf B Biointerfaces **157**:130–137. https://doi.org/10.1016/j.colsurfb.2017.05.056.
40. **Nair RS, Sobhan PK, Shenoy SJ, Prabhu MA, Rema AM, Ramachandran S, Geetha SC, Pratheesh KV, Mony MP, Raj R, Anilkumar TV.** 2022. A porcine cholecystic extracellular matrix conductive scaffold for cardiac tissue repair. J Biomed Mater Res B Appl Biomater. https://doi.org/10.1002/jbm.b.35058.
41. **Park SJ, Kim RY, Park BW, Lee S, Choi SW, Park JH, Choi JJ, Kim SW, Jang J, Cho DW, Chung HM, Moon SH, Ban K, Park HJ.** 2019. Dual stem cell therapy synergistically improves cardiac function and vascular regeneration following myocardial infarction. Nat Commun **10**:3123. https://doi.org/10.1038/s41467-019-11091-2.
42. **Pattar SS, Hassanabad AF, Fedak PW.** 2019. Acellular extracellular matrix bioscaffolds for cardiac repair and regeneration. Front Cell Dev Biol **7**:63. https://doi.org/10.3389/fcell.2019.00063.
43. **Prabhu SD, Frangogiannis NG.** 2016. The biological basis for cardiac repair after myocardial infarction. Circ Res **119**:91–112. https://doi.org/10.1161/CIRCRESAHA.116.303577.
44. **van Putten S, Shafieyan Y, Hinz B.** 2016. Mechanical control of cardiac myofibroblasts. J Mol Cell Cardiol **93**:133–142. https://doi.org/10.1016/j.yjmcc.2015.11.025.
45. **Raj R, Shenoy SJ, Mony MP, Pratheesh KV, Nair RS, Geetha CS, Sobhan PK, Purnima C, Anilkumar TV.** 2021. Surface modification of polypropylene mesh with a porcine cholecystic extracellular matrix hydrogel for mitigating host tissue reaction. ACS Appl Bio Mater **4**:3304–3319. https://doi.org/10.1021/acsabm.0c01627
46. **Rebouças J de S, Santos-Magalhães NS, Formiga FR.** 2016. Cardiac regeneration using growth factors: Advances and challenges. Arq Bras Cardiol **107**:271–275. https://doi.org/10.5935/abc.20160097.
47. **Reddy K, Khaliq A, Henning RJ.** 2015. Recent advances in the diagnosis and treatment of acute myocardial infarction. World J Cardiol **7**:243–276. https://doi.org/10.4330/wjc.v7.i5.243.
48. **Rensen SSM, Doevendans PAFM, van Eys GJJM.** 2007. Regulation and characteristics of vascular smooth muscle cell phenotypic diversity. Netherlands Hear J **15**:100–108.
49. **Revi D, Geetha C, Thekkuveettil A, Anilkumar TV.** 2016. Fibroblast-loaded cholecyst-derived scaffold induces faster

healing of full thickness burn wound in rabbit. J Biomater Appl **30**:1036–1048. https://doi.org/10.1177/0885328215615759.

50. **Revi D, Vineetha VP, Muhamed J, Rajan A, Anilkumar TV.** 2013. Porcine cholecyst-derived scaffold promotes full-thickness wound healing in rabbit. J Tissue Eng **4**:2041731413518060. https://doi.org/10.1177/2041731413518060.
51. **Rieckmann M, Delgobo M, Gaal C, Büchner L, Steinau P, Reshef D, Gil-Cruz C, Horst ENT, Kircher M, Reiter T, Heinze KG, Niessen HW, Krijnen PA, van der Laan AM, Piek JJ, Koch C, Wester HJ, Lapa C, Bauer WR, Ludewig B, Friedman N, Frantz S, Hofmann U, Ramos GC.** 2019. Myocardial infarction triggers cardioprotective antigen-specific T helper cell responses. J Clin Invest **129**:4922–4936. https://doi.org/10.1172/JCI123859.
52. **Robinson KA, Li J, Mathison M, Redkar A, Cui J, Chronos NAF, Matheny RG, Badylak SF.** 2005. Extracellular matrix scaffold for cardiac repair. Circulation **112**:I-135–I-143. https://doi.org/10.1161/CIRCULATIONAHA.104.525436.
53. **Rusu M, Hilse K, Schuh A, Martin L, Slabu I, Stoppe C, Liehn EA.** 2019. Biomechanical assessment of remote and postinfarction scar remodeling following myocardial infarction. Sci Rep **9**:16744. https://doi.org/10.1038/s41598-019-53351-7.
54. **Serpooshan V, Zhao M, Metzler SA, Wei K, Shah PB, Wang A, Mahmoudi M, Malkovskiy AV, Rajadas J, Butte MJ, Bernstein D, Ruiz-Lozano P.** 2013. The effect of bioengineered acellular collagen patch on cardiac remodeling and ventricular function post myocardial infarction. Biomaterials **34**:9048–9055. https://doi.org/10.1016/j.biomaterials.2013.08.017.
55. **Siddiqi S, Sussman MA.** 2014. The heart: Mostly postmitotic or mostly premitotic? Myocyte cell cycle, senescence, and quiescence. Can J Cardiol **30**:1270–1278. https://doi.org/10.1016/j.cjca.2014.08.014.
56. **Suvarna SK, Layton CB, Bancroft JD.** 2013. Connective and other mesenchymal tissues with their stains, p 187–214. Bancroft's theory and practice histological techniques, 7th ed. Oxford, United Kingdom: Churchill Livingstone Elsevier.
57. **Talman V, Ruskoaho H.** 2016. Cardiac fibrosis in myocardial infarction—from repair and remodeling to regeneration. Cell Tissue Res **365**:563–581. https://doi.org/10.1007/s00441-016-2431-9.
58. **Tang J, Su T, Huang K, Dinh PU, Wang Z, Vandergriff A, Hensley MT, Cores J, Allen T, Li T, Sproul E, Mihalko E, Lobo LJ, Ruterbories L, Lynch A, Brown A, Caranasos TG, Shen D, Stouffer GA, Gu Z, Zhang J, Cheng K.** 2018. Targeted repair of heart injury by stem cells fused with platelet nanovesicles. Nat Biomed Eng **2**:17–26. https://doi.org/10.1038/s41551-017-0182-x.
59. **Taylor DA, Parikh RB, Sampaio LC.** 2017. Bioengineering hearts: Simple yet complex. Curr Stem Cell Rep **3**:35–44. https://doi.org/10.1007/s40778-017-0075-7.
60. **Thavapalachandran S, Grieve SM, Hume RD, Le TYL, Raguram K, Hudson JE, Pouliopoulos J, Figtree GA, Dye RP, Barry AM, Brown P, Lu J, Coffey S, Kesteven SH, Mills RJ, Rashid FN, Taran E, Kovoor P, Thomas L, Denniss AR, Kizana E, Asli NS, Xaymardan M, Feneley MP, Graham RM, Harvey RP, Chong JJH.** 2020. Platelet-derived growth factor-AB improves scar mechanics and vascularity after myocardial infarction. Sci Transl Med **12**:eaay2140. https://doi.org/10.1126/scitranslmed.aay2140.
61. **Uchinaka A, Yoshida M, Tanaka K, Hamada Y, Mori S, Maeno Y, Miyagawa S, Sawa Y, Nagata K, Yamamoto H, Kawaguchi N.** 2018. Overexpression of collagen type III in injured myocardium prevents cardiac systolic dysfunction by changing the balance of collagen distribution. J Thorac Cardiovasc Surg **156**:217–226.e3. https://doi.org/10.1016/j.jtcvs.2018.01.097.
62. **Wang Z, Wang Z, Lu WW, Zhen W, Yang D, Peng S.** 2017. Novel biomaterial strategies for controlled growth factor delivery for biomedical applications. NPG Asia Mater **9**:e435. https://doi.org/10.1038/am.2017.171.
63. **Wang Z, Stuckey DJ, Murdoch CE, Camelliti P, Lip GYH, Griffin M.** 2018. Cardiac fibrosis can be attenuated by blocking the activity of transglutaminase 2 using a selective small-molecule inhibitor. Cell Death Dis **9**:613. https://doi.org/10.1038/s41419-018-0573-2.
64. **Wei S, Chow LTC, Shum IOL, Qin L, Sanderson JE.** 1999. Left and right ventricular collagen type I/III ratios and remodeling post-myocardial infarction. J Card Fail **5**:117–126. https://doi.org/10.1016/S1071-9164(99)90034-9.